Silicon (2024) 16:3405–3415
https://doi.org/10.1007/s12633-024-02933-w

RESEARCH

Fabrication and Characterization of Thermally Insulating Polyurethane-Silica Aerogel Composite for Cryogenic Application

I. Nuhu[1,2] · Z. A. A. Halim[1] · N. Awang[3] · M. A. M. Yajid[1] · W. F. F. Wan Ali[1]

Received: 26 November 2023 / Accepted: 25 February 2024 / Published online: 4 March 2024

Abstract

Polyurethane-silica aerogel (PUSA) composites have been synthesized in this study for thermal insulation applications. Silica Aerogel (SA) was synthesized from sodium silicate solution through a standard sol–gel process and ambient pressure drying. Previous research has shown that combining PU with SA in a composite causes brittle fracture at lower temperatures. This study proposes that PU was re-formulated with ethylene glycol (EG) as an antifreeze and chain extender to enhance the mechanical properties. In this experiment, different composites were produced having different SA concentrations (0.5 wt.%, 1.0 wt.%, 1.5 wt.%, and 2.0 wt.%). The glass transition temperature (T_g) of the PUSA composites as conducted by Differential Scanning Calorimetry (DSC) between 0 to -80 ℃ reveals the shift in T_g by as much as 12% with SA addition between 0.5–2.0 wt. %. PUSA composite with 1 wt.% SA demonstrates the highest compressive strength (0.56 MPa), while composite with 1.5 wt.% SA exhibited the lowest thermal conductivity (0.2 W/mK). PUSA composites containing 1.0–1.5 wt.% SA exhibited optimum mechanical strength and thermal insulation properties.

Keywords Polyurethane · Silica Aerogel · Composite · Compressive strength · Glass transition temperature

1 Introduction

Polyurethane (PU) foams are versatile polymers that thrive in diverse insulation applications. Tailored to meet specific needs, they boast exceptional mechanical strength and stability across a wide temperature range, making them prime candidates for cryogenic insulation in liquefied natural gas (LNG) pipelines and cargo containment systems (CCS) [1]. Yet, for such demanding environments, PU foams alone lacks the robust compression resistance needed to withstand cryogenic impact forces. Numerous efforts have tackled this challenge including nanoparticle reinforcement [2]. Introducing chopped glass fibres yielded rigid polyurethane foam (RPUF) with enhanced mechanical properties, promising for LNG/CCS insulation. However, RPUF suffers from compromised thermal insulation due to the high thermal conductivity of glass fibres (15–17 times that of PU foam). Moreover, PU foam itself undergoes a concerning decline in cryogenic strength, fracturing readily at -163 °C under compression testing. Conversely, RPUF's impregnated glass fibre preserve structural integrity at cryogenic temperatures [3], albeit at higher production costs [4]. Similar limitations arise with other approaches: graphene oxide improves Young's modulus but falls short at cryogenics [5], while OMMT fillers enhance strength but raise thermal conductivity [6, 7]. PU foam-Kevlar Pulp composites offer enhanced insulation and strength at specific ratios, but rising fibre content compromises cryogenic performance due to increased porosity [8, 9].

Silica aerogel (SA), known for its remarkable insulation properties, presents itself as a potential cryogenic material. However, its lack of compressive strength hinders standalone applications. While promising studies show that adding 1% SA particles into PU foam can enhance strength and reduce conductivity compared to pure PU foam, higher concentrations negatively impact cell structure and ultimately hinder thermal performance

✉ M. A. M. Yajid
azizi@utm.my

[1] Department of Materials, Manufacturing and Industrial Engineering, Faculty of Mechanical Engineering, Universiti Teknologi Malaysia, 81310 Johor Bahru, Malaysia

[2] Centre for Renewable Energy Research, Umaru Musa Yar'adua University, Katsina, Nigeria

[3] Plant Engineering Technology (PETECH), Malaysian Institute of Industrial Technology, Universiti Kuala Lumpur, 81750 Johor Bahru, Johor, Malaysia

[10]. Similar issues arise with chopped glass fibers in PU foam, where optimal loading remains crucial to manage conductivity [11]. Another study found that grinded SA can rupture the PU foam cells upon incorporation, further exacerbating thermal conductivity [12]. Rigid and flexible PU foams, although efficient and economical, exhibit high glass transition temperatures compared to LNG's operating temperature (-163 °C). This renders them brittle and unstable at cryogenic conditions [13, 14]. Nanoparticle additions, while reported to increase mechanical strength, often sacrifice thermal insulation leading to thicker and heavier insulation layers [11, 15]. Although previous studies have demonstrated the promising thermal insulation properties of PU-SA composites, these materials still exhibit detrimental brittleness and fracturing at cryogenic temperatures due to a significant mismatch between their glass transition temperature (T_g) and the operating conditions [16].

This research proposes that the key to overcoming this limitation lies in modifying the PU foam itself before incorporating SA. This approach stands in contrast to past attempts focused solely on incorporating reinforcing materials like chopped glass fibres or nanoparticles, which often compromise thermal insulation or increase production costs [3, 5]. This study takes a novel approach to optimize PU-SA composites for cryogenic insulation by incorporating ethylene glycol (EG) as a dual-function agent: acting as both an antifreeze to improve cryogenic stability and a chain extender to fine-tune the microstructure. Additionally, distilled water is employed as a clean and sustainable blowing agent [17, 18]. This unique combination, unexplored in prior research, aims to address the fundamental cause of cryogenic instability in PU foams, paving the way for robust and efficient cryogenic insulation solutions.

2 Materials and Methods

2.1 Materials

The PU employed in this study was semi-rigid hydrophobic (PU-301, Impex Corporation, Nagar, Bangalore) with a density of 1.0 g/cm^3 and a viscosity of 2800 ± 200 centipoise at 25 ℃. It exhibited a hydroxyl value ranging from 510 to 537 KOH/g. EG as obtained from Sigma Aldrich was used as chain extender and anti-freezing agent. Acetic acid and sodium silicate solution with a density of 1.35 g/cm^3 were purchased from Supelco Merck Darmstadt, Germany. Trimethylchlorosilane (TMCS 98%, Sigma-Aldrich) with a density of 0.86 g/cm^3 was used as silylating agent. N-Hexane (C_6H_{14}), with a density of 0.66 g/cm^3 was acquired from Merck Co., Germany. Ethanol was purchased from V-Chem Laboratories Pvt. Ltd., Malaysia. Deionized water was used throughout the process. All reagents utilized were of analytical grade.

2.2 Methods

2.2.1 Silica Aerogel Synthesis

SA was synthesized from sodium silicate as illustrated in Fig. 1. The precursor was diluted with deionized water in a volume ratio of 1:3. Acetic acid was then added dropwise to the solution leading to sol–gel transition at pH 5.0–5.5. The resulting gel was aged in distilled water bath at 60–70 ℃ for 48 h as per the method described in [19]. Subsequently, the aged sols were washed to remove soluble salts before undergoing solvent exchange in a Soxhlet extractor. During solvent exchange process, pore water within the silica gels was replaced by ethanol through cyclic process for 72 h,

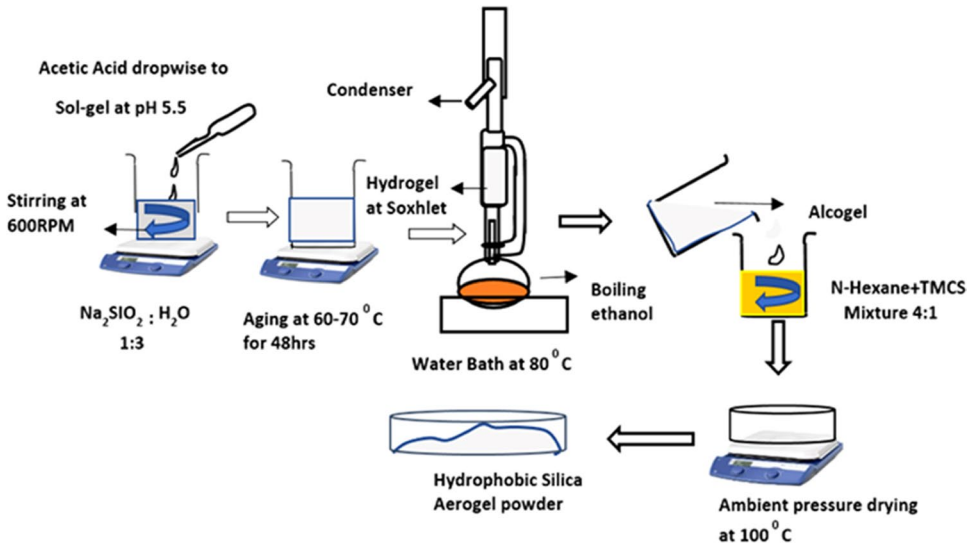

Fig. 1 Process of SA synthesis from sodium silicate via ambient pressure drying

yielding silica alcogels. Then, the silica alcogels were surface modified to renders hydrophobicity on their surfaces. Surface modification was achieved by immersing the silica alcogel in a silylating mixture containing TMCS and N-Hexane in a 2:8 volume ratio. Specifically, 100 ml of alcogel was immersed in 100 ml of the mixture and gently stirred for 2 h, following the method outlined in [20]. To remove residual hydrochloric acid (HCl) byproduct and unreacted TMCS, the gel was thoroughly rinsed with fresh N-hexane. Subsequently, the surface-modified alcogels underwent drying on a hot plate at 100 °C. This treatment evaporated the pore solvents, yielding the final hydrophobic SA.

2.2.2 Polyurethane Reformulation and Composite Casting

Table 1 presents various formulations of PU and PUSA composites with varying amounts of SA (in wt%). Two control samples (pristine PU composites) were prepared: PUH2, without EG modification, and PUSA0, without SA. EG modification was applied to other PU composites to optimize pore sizes and structural strength [21]. Composite components were thoroughly mixed using a mechanical stirrer for 60 s in a flat-bottom polyethylene beaker (500 ml). The resulting blend was then poured into an aluminium cuboid with internal dimensions of 60 mm × 60 mm × 40 mm (length × width × breadth). The homogenous mixture was sealed and left under ambient conditions for 48 h. The composite casting process is depicted in Fig. 2, and the physical appearance of the casted composites is shown in Fig. 3.

Table 1 Designation of composite samples and their compositions

Sample	PUF 301 (mL)	Proportion of SA (wt. %)	EG (mL)	Distilled water (mL)
PUH2	15	0	0	2
PUSA0	15	0	1	2
PUSA1	15	0.5	1	2
PUSA2	15	1.0	1	2
PUSA3	15	1.5	1	2
PUSA4	15	2.0	1	2

2.3 Characterization

2.3.1 Compressive Test

Cuboid samples of PUSA composites, measuring 60 × 60 × 40 mm, were subjected to compressive strength analysis using an Instron 4467 Universal Testing Machine (UTM) under ambient conditions. The machine operated at a crosshead speed of 2.5 mm/min, adhering to ASTM D695 standards. Strain data acquired from the test was used to establish strain–stress relationships.

2.3.2 Chemical Analysis

The molecular structure of SA, PU and their composites were characterized using Fourier Transform Infrared (FT-IR) spectroscopy. Material spectra of the samples were recorded on

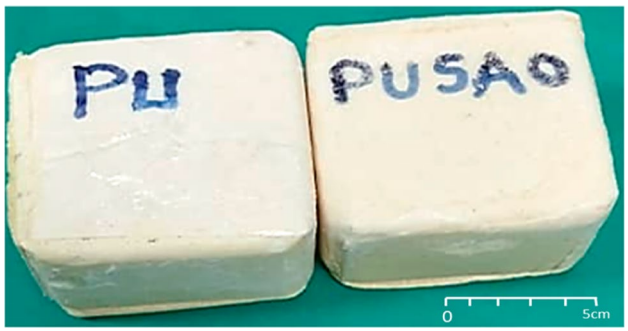

Fig. 3 Photographs of pristine PU composites (PUH2 and PUSA0)

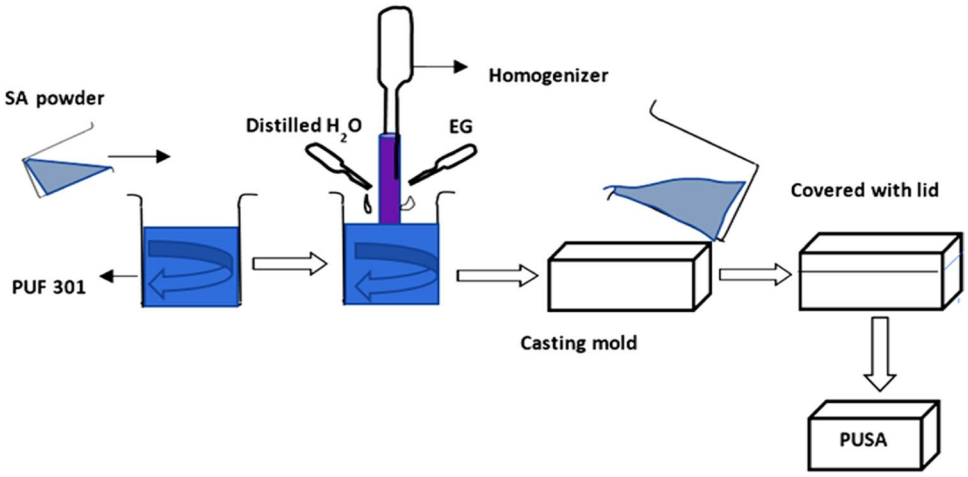

Fig. 2 Schematic of process flow for fabrication of PUSA composites

a Perkin Elmer 2000 attenuated total reflection (ATR)-FTIR instrument within the range of 400–4000 cm^{-1} at a resolution of 5 cm^{-1}.

2.3.3 Composite's Density and Porosity

Sample's densities were determined gravimetrically using an analytical balance and sample volume measured by water displacement (accuracy ± 0.05 cm^3). Average weight from five replicates and GB/T 6343–2009 standards calculated individual and composite densities. The composite's porosity was subsequently computed by utilizing its theoretical density and skeletal density, as determined by the rule of mixtures, following the methodology outlined in [22]. All measurements were repeated five times and averaged.

2.3.4 SEM–EDX Analysis

The morphology and the dispersion of SA within the PU matrices were observed under Scanning Electron Microscope (SEM, Hitachi SU3400) and further analyzed using energy dispersive X-ray (EDX, Oxford Instrument). Prior to observation, the SEM samples measuring 10 mm in diameter and 3 mm in thickness were subjected to surface polishing and gold coating.

2.3.5 Thermal Conductivity

Thermal conductivity measurement of the PUSA composites was conducted in accordance to ASTM C177 standards (Fig. 4). Samples with dimensions of 25 mm diameter and 5 mm thickness were prepared and mounted between a heating cylinder and a heat dissipater. A heating voltage of 25 kV was applied and both the heating (T1) and dissipating (T2) temperatures were recorded at minute intervals using TC-08 Thermocouple Data Logger (Pico Technology, UK). Thermal conductivity (k) was subsequently calculated based on Eqs. (1) and (2).

$$Q = \dot{m} \times C \times \Delta T \tag{1}$$

$$k = 4.1\frac{QL}{dt} \tag{2}$$

Whereby,

$\dot{m}$	water flow rate
C	Water heat capacity
Q	Heat transfer into the sample
L	Thickness of sample
A	Sample surface area
ΔT	Difference between water inlet and outlet temperature
dt	Difference between heating and dissipating temperature
k	the material overall thermal conductivity

2.3.6 Heat Calorimetry

Differential Scanning Calorimetry (DSC, Mettler-Toledo DSC822C/600) was employed to assess the shift in the material's T_g and the alterations in thermal transitions resulting from the incorporation of SA into the PU. For the analysis, 10 g of powdered material was utilized and subjected to heating at a rate of 10 °C min^{-1} The temperature range spanned from -80 °C to 150 °C with a continuous flow of 40 L/min N_2 gas.

3 Results and Discussion

3.1 Physical and Chemical Properties of SA

Table 2 presents the properties of the synthesized SA which was utilized in the study. The hydrophobic nature of the material is confirmed by the FTIR analysis in Fig. 5, The peaks observed in the spectra at approximately 800 cm^{-1}

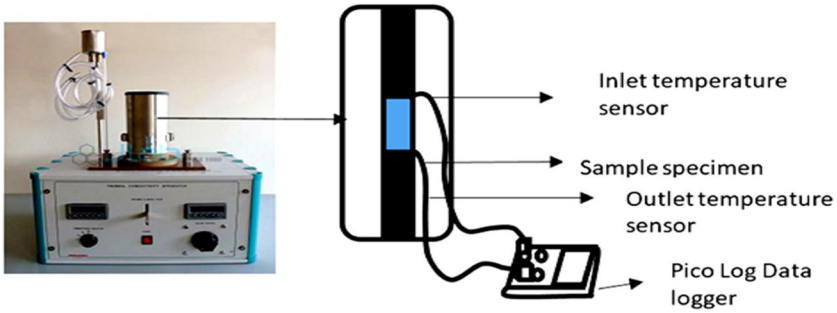

Fig. 4 Thermal conductivity measurement apparatus with a schematic illustrating a set-up in the heating chamber

Table 2 Physical properties of the synthesized SA

Property	Value
Bulk Density	0.109 g/cm^3
Surface area	500–600 m^2/g
Particle size	0.2–2 mm
Porosity	95%

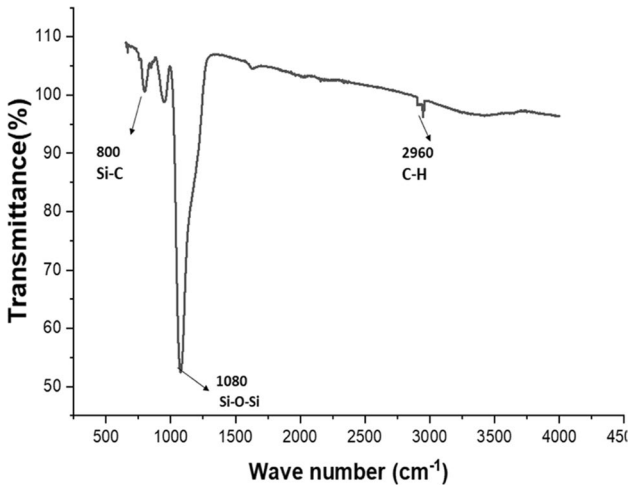

Fig. 5 FTIR spectrum of the synthesized SA

and 2960 cm^{-1} represent the Si–C and C–H bonds present in TMCS, indicating the formation of a hydrophobic surface. The absence of peaks associated with hydroxyl groups at 3400 cm^{-1} and 1630 cm^{-1} was due to hydrophobization of the SA surface [23]. Figure 6 demonstrates the physical form of the SA sample and its internal porous structures (SEM images) after ambient pressure drying.

3.2 SEM–EDX Analysis of PUSA Composites

SEM analysis revealed the influence of SA contents on the generation and size of cell pores in the matrix. In Fig. 7, it is observed that matrix homogeneity is associated with particle concentration. Low concentrations (Fig. 7a, b) of SA favour the generation of regular, circular, and closed pores, while high concentrations beyond the critical value cause pore degeneration and cell rupture. SEM confirms the rupture of some cells in Fig. 7c, d, and e for PUSA composites containing 1.0 to 2.0 wt.% of SA. Furthermore, the presence of irregular and damaged cells, caused by high particle loading exceeding the critical value, diminishes the matrix's mechanical properties, as the cell walls that provide structural support and strength are negatively affected, as evident in Fig. 7d and e. In Fig. 7b and c, it can be observed that the pores are distinctly circular with a reduced cell size compared to Fig. 7d and e. It has a more homogeneous particle dispersion with circular pores comparatively. Similarly, as the loading increased to 1 wt.%, the matrix remained homogeneous with an increased cell size compared to 0.5 wt.%. However, as the loading increased, the cell walls ruptured, and the cell geometry became distorted, displaying changes to elliptical and disfigured with non-uniform particle dispersion, as evident in Fig. 7d and e. During the forming process, the more air included, the higher the nucleation effect [24]. Similarly, the cell formation process is affected by the introduction of nanoparticles altering the matrix morphology compared to the pristine matrix. At optimal loading cell morphology is altered without significant distortion and ruptures, which could lead to the loss of desired composite properties [25, 26].

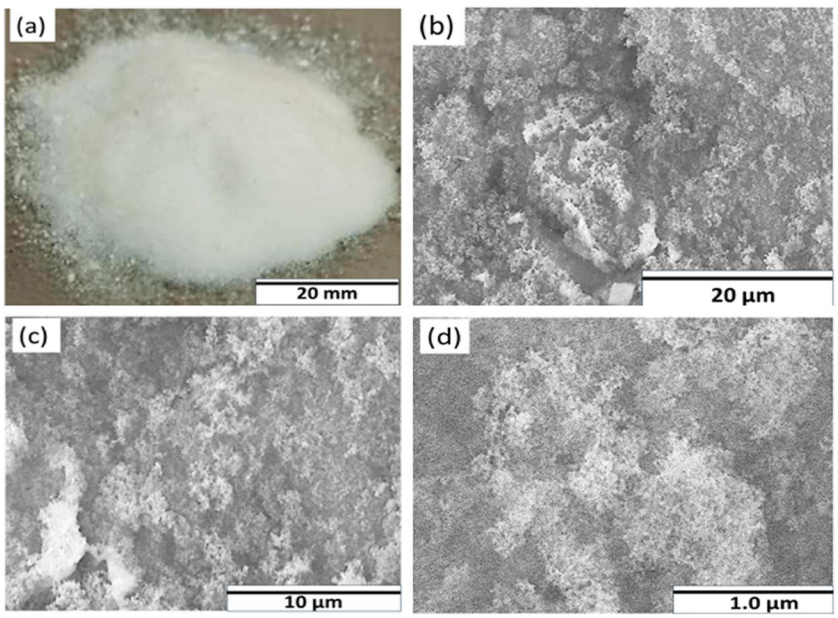

Fig. 6 **a** Photograph of the synthesized SA (**b**) SEM micrograph at Mag = 2000× (**c**) SEM micrograph at Mag = 5000× (**d**) SEM micrograph Mag = 10,000×

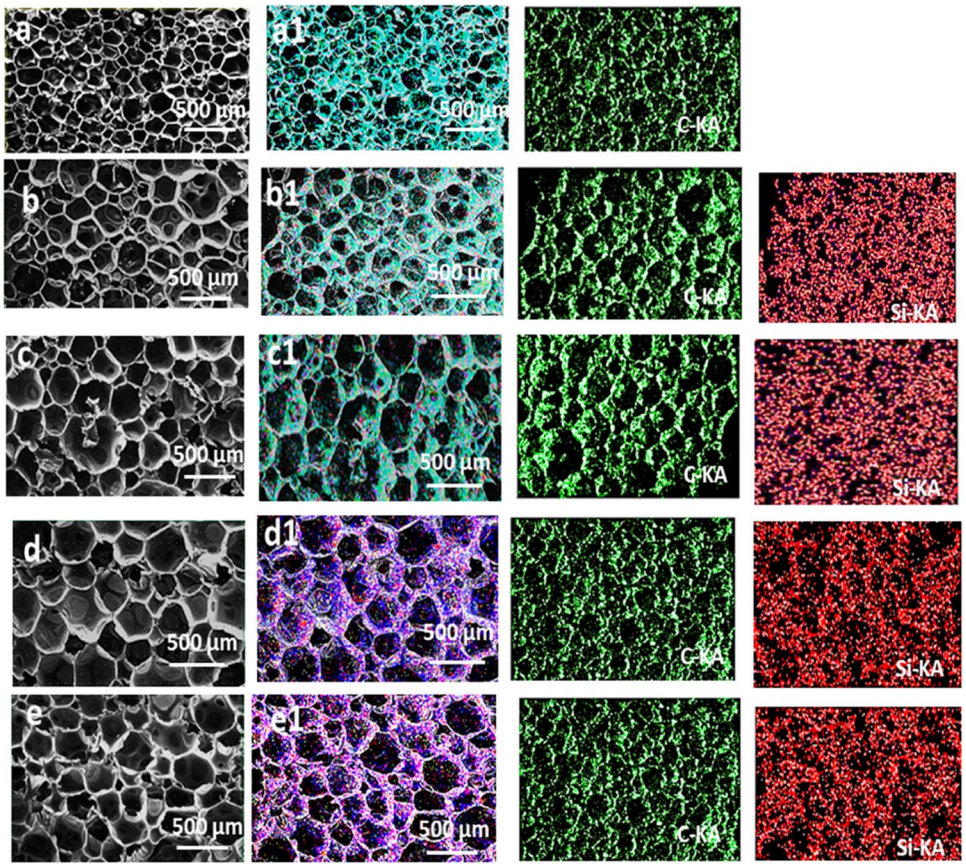

Fig. 7 SEM micrograph and EDX Mapping of sample (**a**) PUSA0 with 0 wt.% of SA (**b**) PUSA1 with 0.5 wt.% of SA (**c**) PUSA2 with 1 wt.% of SA (**d**) PUSA3 with 1.5 wt.% of SA and (**e**) PUSA4 with 2.0 wt.% of SA respectively

3.3 Densities of PUSA Composites

Figure 8 illustrates the variation in composite densities with varying SA content. Initially, it was assumed that composite density would diminish with increasing SA content. However, contrary to expectations, the incorporation of low SA particles led to an elevation in material density. This phenomenon can be attributed to the involvement of SA particles in the foaming process, contributing to densification. Nevertheless, a decrease in density was observed as the SA content increased from 1.5 wt.% to 2.0 wt.%. The composite reached its maximum density at 1.5 wt.%. Subsequently, as SA content increased further, the density decreased. This decline can be rationalized by the rupture of cell pores as particle concentrations exceeded the threshold for effective nucleation. Consequently, an increase in SA content resulted in the formation of cell pores on the composite's surface, leading to a reduction in density.

The cellular structure of the PU consists of an intact lattice framework surrounded by gas-containing pores. Under load, internal forces acting on the PU's cell walls maintain its foam's shape [27]. However, when stress surpasses the elastic limit, the cell walls bend and eventually tear, leading to rupture. The presence of closed cell structures, achieved at low SA content, enhances heat insulation performance

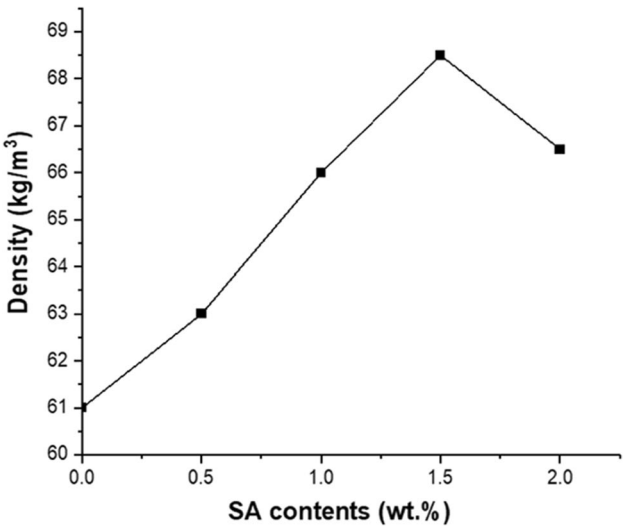

Fig. 8 Variation of Composite density with increase in wt. % of SA

of the PUSA composites. Conversely, high SA content may disrupt PU foam homogeneity and diminish functionality [28]. Excessive SA incorporation, while promoting closed cell formation, can reduce composite homogeneity and compromise function. The intersection of numerous cells

as structural elements forms struts with relatively small strut areas. Moreover, as SA content increases, cell structure irregularities emerge [29]. The extremely low density of SA inhibits consistent cell formation and hampers particle dispersion, impeding homogeneous cell creation as solution viscosity rises. Furthermore, concerning materials for cryogenic insulation, the impact of applied load on cellular degeneration outweighs exposure to cryogenic liquids or seawater [30].

3.4 Molecular Structure of PUSA Composites

Structural changes in the PUSA composites were investigated using FT-IR spectroscopy, as depicted in Fig. 9 and further described in Table 3. These changes, encompassing alterations in orientation and crystalline shape, were confirmed through attenuated total reflectance measurements of the PU component. PU contains the -NHCOO- group, indicative of the urethane bond, with the -OH group as an active hydroxyl group and the isocyanate group (-N=C=O) serving as another active group [31]. Vibrations associated with C-O bonds at 1720 cm^{-1}, N–H vibrations at 1530 cm^{-1}, and symmetric and antisymmetric stretching vibrations of C–O–C at 1230 cm^{-1} and 1070 cm^{-1} were observed [16]. An increase in peak heights and area was observed as aerogel contents increased from 0.5–1.5 wt.%. However, these trends decreased when contents increased to 2 wt.%. Interestingly, the length of the hydroxyl group stretching vibrations at 3750 cm^{-1} was longer in all composite samples compared to the sample without SA (0 wt.%). The presence of SA was further confirmed by the asymmetric CH_3 stretching vibrations at 2930 cm^{-1} from $SiCH_3$, which is the only component of SA. The presence of EG in the composite was confirmed by the O–H stretching vibration at

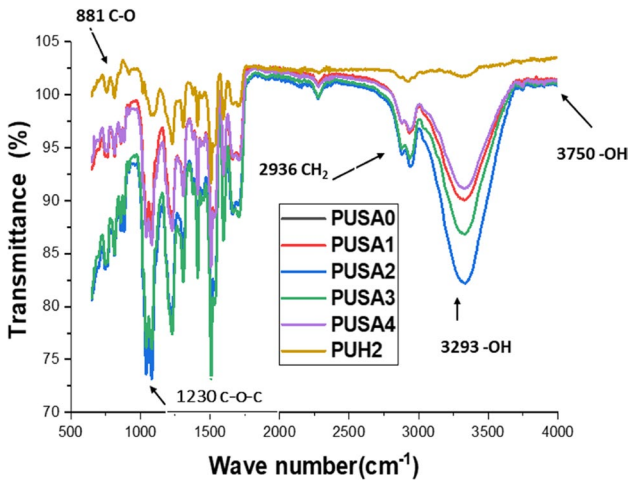

Fig. 9 Molecular structure of the composite samples as depicted by FTIR spectra

3293 cm^{-1}, νC-H symmetric and asymmetric stretching at 2936 and 2874 cm^{-1} of the –CH2 groups [32]. Additionally, the νC-O symmetric and asymmetric stretching vibration was observed at 1413 cm^{-1} (a weak band between 1500 and 1400 cm^{-1}) in the fingerprint's region. Within a strong band, a vibration was observed at 1082 and 1036 cm^{-1}, and a rocking vibration at 881 cm^{-1} in agreement with [33].

3.5 Thermal analysis of PUSA composites

3.5.1 DSC

The DSC analysis conducted on the composite samples reveals a notable shift in the T_g influenced by the addition of EG. A significant shift of approximately 11.9% is observed, from -51.34 ℃ in the pristine PU to -57.46 ℃ with the incorporation of EG. However, upon adding SA, the transition temperature shifts slightly in a positive direction due to the amorphous nature of SA. Furthermore, as SA contents increase from 0.5–2.0 wt.%, the matrix T_g shift becomes nearly negligible. This phenomenon could be attributed to the anti-freezing activity of EG, which exhibits less effect with the addition of SA within the tested concentrations, as indicated in Table 4. Interestingly, composites containing SA exhibit a stable heat flow. The DSC thermogram depicted in Fig. 10 illustrates the transition of sample PUSA0, exhibiting a lower T_g of -57.46 ℃ compared to -51.34 ℃ observed for pristine PUH2 (without SA and EG). This difference suggests the influence of EG in shifting the material's T_g. Similarly, the presence of SA particles affects the stable heat flow of the composite within the tested temperature range. This influence is evident in the more parallel curves displayed by composites with SA (PUSA1, PUSA2, PUSA3 and PUSA4) compared to PUSA0. This study recorded a lower T_g of -57.46 ℃, indicating improved composite stability at lower temperatures, compared to the lowest T_g of -47 ℃ as reported in [34], demonstrating further enhancement in composite cryogenic stability.

3.5.2 Thermal Conductivity

The thermal conductivity test was conducted 12 days after casting the composites to allow for the stabilization of the blowing agent, which may influence thermal conduction measurements [35]. The inclusion of SA resulted in a reduction of thermal conductivity, indicating improved thermal insulation, as depicted in Fig. 11. This decrease in thermal conductivity showed a consistent trend as SA content increased from 0.5 to 1.0 and 1.5 wt.%. However, when the SA content reached 2.0 wt.%, there was an observed increase in thermal conductivity. Notably, the sample containing 1.5 wt.% of SA among the tested samples exhibited the lowest conductivity. These findings suggest that the thermal

Table 3 Samples FTIR Spectra and their peak assignment

Wavelength (cm^{-1})	Peak Assignment
881	C-O symmetric and asymmetric rocking stretching vibration
1082–1036	C-O symmetric and asymmetric strong vibration stretching vibration
1070	C–O–C asymmetric stretching vibration
1270	C–O–C asymmetric stretching vibration
1230	C–O–C asymmetric stretching vibration
1413	C-O symmetric and asymmetric stretching vibration
1530	N–H
1720	C = O
2874	C-H asymmetric stretching of the CH_2 group
2930	C–H stretching vibration
2874	$–CH_2$ asymmetric stretching
2936	$–CH_2$ C-H symmetric
3294	O–H stretching vibration
3750	-OH hydroxyl group stretching vibrations

Table 4 Glass transition temperature (T_g) of the sample composites

Composite Sample	Onset T_g(℃)	$T_{g\ Midpoint}$ (℃)
PUH2	-51.34	-48.74
PUSA0	-57.46	-54.18
PUSA1	-56.78	-53.42
PUSA2	-56.80	-54.23
PUSA3	-55.96	-53.60
PUSA4	-56.47	-54.23

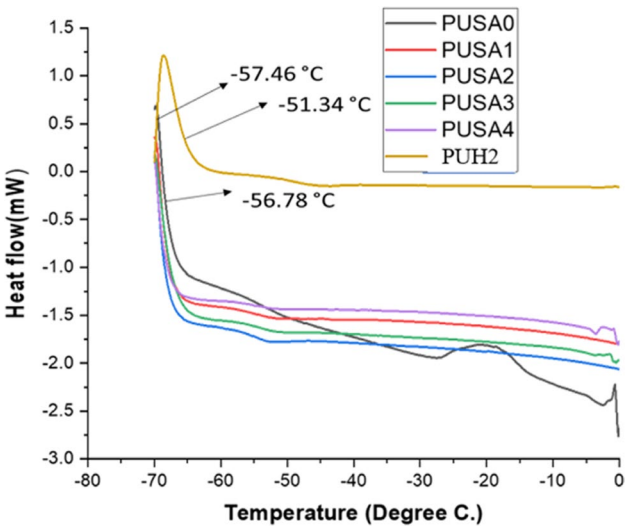

Fig. 10 DSC thermogram of pristine PU samples (PUSA0 and PUH2) and PUSA composites

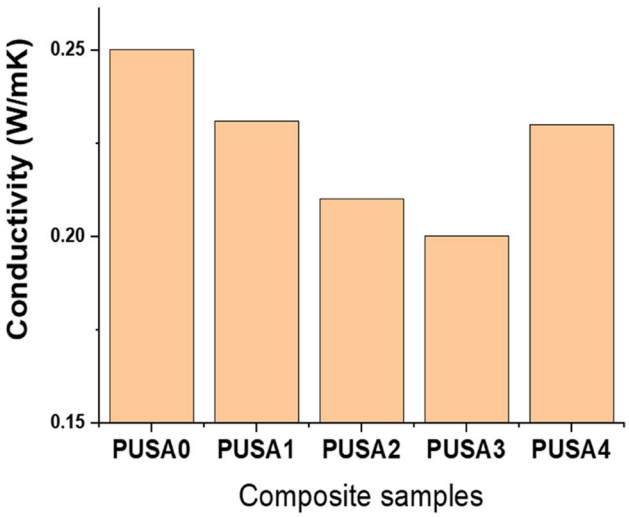

Fig. 11 Thermal conductivity of PUSA composites at different SA loadings

insulation of the PUSA composite reached its peak at 1.5 wt.% SA. Beyond this concentration, thermal insulation appears to decline, possibly due to SA particles disrupting the porous structure of PU. It was anticipated that adding high contents of particles with ultra-low conductivity would reduce the overall conductivity. However, an increase in particle quantity resulted in an increase in material thermal conductivity. This rise in heat conductivity was attributed to modifications in cell shape. In the matrix, small, uniform, and rounded cells performed better in terms of thermal insulation than large and irregular ones. PUSA3 (1.5 wt.% SA) displayed the least thermal conductivity among the samples tested, showing a reduction of approximately 13% compared to the same composition of the composite reported in [36].

3.6 Compressive Strength

Figure 12 displays the stress–strain curves obtained from the compressive test of the composites. The study reveals that

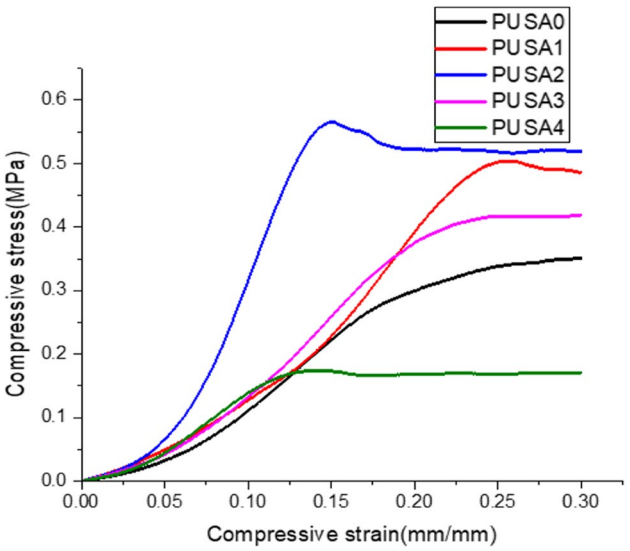

Fig. 12 Compressive stress–strain curves of the PU-SA composites

the highest compressive strength of 0.56 MPa was achieved at 1 wt.% of SA. In comparison, the 1.5 wt.% SA composite demonstrated a good compressive strength of 0.50 MPa, but it exhibited a higher nominal strain compared to the 1 wt.% composite. It was observed that 1 wt.% SA provided the highest compressive strength due to the presence of uniform cells with thicker cell walls that support compressive load. Normally, cell walls provide the material's compressive strength and structure as they oppose each other [35]. The use of higher SA contents led to the deterioration of cell structures and decreased mechanical strength in the composite. The compressive strength demonstrated by the material could be explained as the expansion of the damaged cells found consistent with [37].

Meanwhile, Fig. 13a illustrates the compressive strength of the composite material as a function of various levels of SA loading. It is evident from the graph that the sample designated as PUSA2, containing 1 wt.% SA loading, demonstrates the highest compressive strength. This observation aligns with previous study [29]. The strength exhibited by the material could be correlated to its matrix morphology. At lower loading levels (0–1 wt.%), the particles participate in uniform cell formation, leading to an increase in compressive strength without significant changes in cell geometry. However, visible changes in morphology occur as the loading exceeds 1 wt.%. Figure 13b shows a micrograph of PUSA2 with the highest compressive strength and PUSA4 with the lowest compressive strength among the samples tested. PUSA2 exhibits a more circular cell geometry (labeled C1) with uniform particle dispersion compared to relatively disfigured cells in PUSA4 (labeled C2). The high compressive strength demonstrated by PUSA2 indicates the

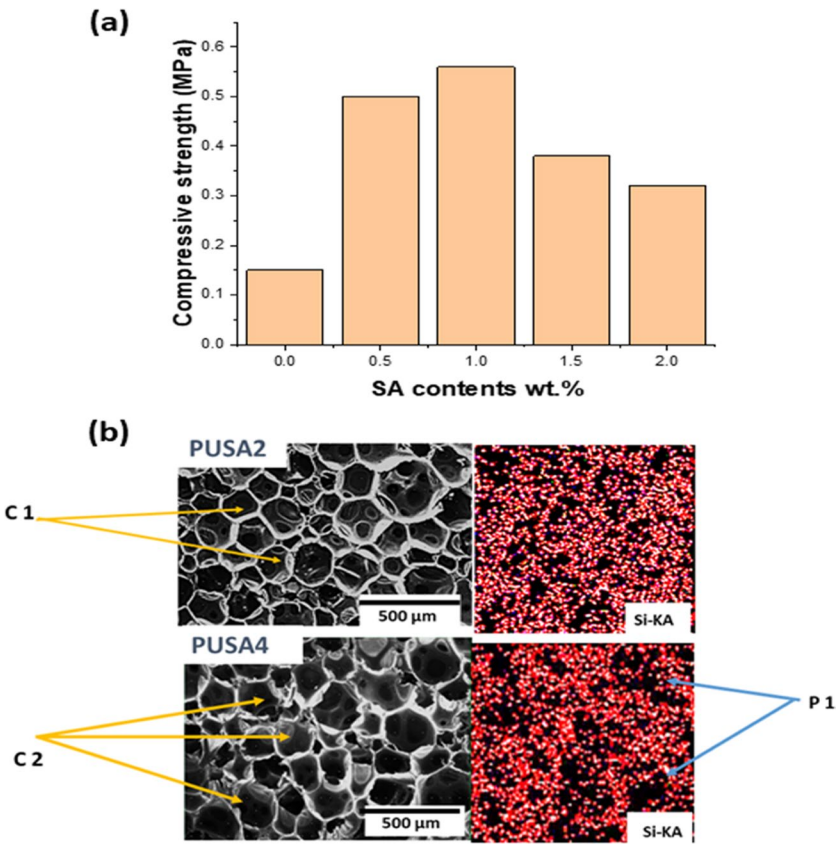

Fig. 13 Compressive behaviour of PUSA composites (**a**) Influence of SA contents on composite's compressive strength (**b**) SEM–EDX analysis of PUSA2 and PUSA4 showing a change of cell geometry and porosity due to SA content

presence of uniform cells that support compressive loads, while PUSA4 demonstrates weaker strength, suggesting the presence of non-uniform cells with a more porous morphology (labeled P1), a behavior attributable to the relative increase in non-homogeneity of SA particle dispersion.

4 Conclusion

This study investigates the influence of SA particles on the mechanical and thermal properties of PU composites. PU, optimized with EG as an antifreeze, forms the base composite. The addition of EG induces a shift in the composites' T_g, while the incorporation of SA enhances the thermal insulation properties of PU. This T_g shift, induced by EG, signifies improved composite stability at cryogenic temperatures. Previous research suggested 1 wt.% SA loading as optimal for both compressive and thermal properties. However, our findings diverge: while compressive strength aligns with previous studies, 1.5 wt.% SA emerges as optimal for thermal properties in this investigation. The composite exhibiting high compressive strength would be preferable in cargo containment systems and applications subject to loading, whereas PUSA3, demonstrating optimal thermal insulation, would be advantageous in cryogenic insulation systems.

Acknowledgements The authors would like to thank the Ministry of Education Malaysia (MOE), Universiti Teknologi Malaysia (UTM) and Faculty of Mechanical Engineering, for providing research facilities and financial support under Grants: UTM-Transdisciplinary Research (TDR) vot Q.J130000.3551.06G6606G66, UTM-Fundamental Research (UTM-FR) vot Q.J130000.2551.20H66 and UTM-High Impact Research Grant (HIR) vot Q.J130000.2551.20H6604G38.

Author contributions I. Nuhu Experimental Work and Manuscript Writing. Z.A.A Halim Review of manuscript and analysis. N. Awang conceptualization and Data analysis. M.A.M Yajid Design of experiment and conceptualization. W.F.F Wan Ali Supervision of experimental work and Data analysis.

Funding This work was supported by Ministry of Education Malaysia (MOE) (Grant numbers: UTM-Transdisciplinary Research (TDR) vot Q.J130000.3551.06G6606G66, UTM-Fundamental Research (UTM-FR) vot Q.J130000.2551.20H66 and UTM-High Impact Research Grant (HIR) vot Q.J130000.2551.20H6604G38.

Data Availability No datasets were generated or analysed during the current study.

Declarations

Ethics Approval Not Applicable.

Consent to Participate Not Applicable.

Consent for Publication All the authors have complete consent for publication.

Competing Interests The authors declare no competing interests.

References

1. Sápi Z, Butler R (2020) Properties of cryogenic and low temperature composite materials – A review. Cryogenics (Guildf). 111(November 2019):103190. https://doi.org/10.1016/j.cryogenics.2020.103190
2. Liu F, Deng S, Zhang J (2017) Mechanical Properties of Epoxy and Its Carbon Fiber Composites Modified by Nanoparticles. J Nanomater 2017:14–16. https://doi.org/10.1155/2017/8146248
3. Park SB, Lee CS, Choi SW, Kim JH, Bang CS, Lee JM (2016) Polymeric foams for cryogenic temperature application: Temperature range for non-recovery and brittle-fracture of microstructure. Compos Struct 136:258–269. https://doi.org/10.1016/J.COMPSTRUCT.2015.10.002
4. Kumar M, Kaur R (2017) Glass fiber reinforced rigid polyurethane foam: Synthesis and characterization. E-Polymers 17(6):517–521. https://doi.org/10.1515/epoly-2017-0072
5. Wan T, Chen D (2018) Mechanical enhancement of self-healing waterborne polyurethane by graphene oxide. Prog Org Coat 121(October 2017):73–79. https://doi.org/10.1016/j.porgcoat.2018.04.016
6. Yufei C, Yang H, Qiwang D, Xiwang Z, Zhang Q (2015) Preparation and properties of OMMT/PU composites. Adv Mater Sci Eng 2015. https://doi.org/10.1155/2015/715879
7. Członka S, Kairytė A, Miedzińska K, Strakowska A, Adamus-Włodarczyk A (2021) Mechanically strong polyurethane composites reinforced with montmorillonite-modified sage filler (Salvia officinalis l.). Int J Mol Sci 22(7). https://doi.org/10.3390/ijms22073744
8. Oh J-H, Bae J-H, Lee J-M (2018) The effects of Kevlar pulp on polyurethane foam for cryogenic temperature. J Soc Nav Archit Korea 55(6). https://doi.org/10.3744/snak.2018.55.6.514
9. Singh T, Pruncu CI, Gangil B, Singh V, Fekete G (2020) Comparative performance assessment of pineapple and Kevlar fibers based friction composites. J Mater Res Technol 9(2):1491–1499. https://doi.org/10.1016/j.jmrt.2019.11.074
10. Hasan MA, Sangashetty R, Esther ACM, Patil SB, Sherikar BN, Dey A (2017) Prospect of thermal insulation by silica aerogel: a brief review. J Inst Eng Ser D 98(2):297–304. https://doi.org/10.1007/s40033-017-0136-1
11. Kim JD, Kim JH, Lee DH, Yeom DJ, Lee JM (2021) Synthesis and investigation of cryogenic mechanical properties of chopped-glass-fiber-reinforced polyisocyanurate foam. Materials (Basel) 14(2):1–18. https://doi.org/10.3390/ma14020446
12. Dourbash A, Buratti C, Belloni E, Motahari S (2017) Preparation and characterization of polyurethane/silica aerogel nanocomposite materials. J Appl Polym Sci 134(8). https://doi.org/10.1002/app.44521
13. Stirna U, Beverte I, Yakushin V, Cabulis U (2011) Mechanical properties of rigid polyurethane foams at room and cryogenic temperatures. J Cell Plast 47(4):337–355. https://doi.org/10.1177/0021955X11398381
14. Greene JP (2021) Microstructures of polymers. Automot Plast Compos. 27–37. https://doi.org/10.1016/b978-0-12-818008-2.00009-x
15. Hwang BK, Kim SK, Kim JH, Kim JD, Lee JM (2020) Dynamic compressive behavior of rigid polyurethane foam with various densities under different temperatures. Int J Mech Sci 180. https://doi.org/10.1016/j.ijmecsci.2020.105657
16. Kim JH, Ahn JH, Kim JD, Lee DH, Kim SK, Lee JM (2021) Influence of silica-aerogel on mechanical characteristics of

polyurethane-based composites: Thermal conductivity and strength. Materials (Basel) 14(7). https://doi.org/10.3390/ma14071790
17. Park SB, Choi SW, Kim JH, Bang CS, Lee JM (2016) Effect of the blowing agent on the low-temperature mechanical properties of CO2- and HFC-245fa-blown glass-fiber-reinforced polyurethane foams. Compos Part B Eng 93:317–327. https://doi.org/10.1016/j.compositesb.2016.03.008
18. Son YM, Kim JD, Choi SW, Kim JH, Her NY, Lee JM (2019) Synthesis of polyurethane foam considering mixture blowing agents for application to cryogenic environments. Macromol Mater Eng 304(11). https://doi.org/10.1002/mame.201900294
19 Abdul Halim ZA, Mat Yajid MA, Idris MH, Hamdan H (2018) Dispersion of polymeric-coated–silica aerogel particles in unsaturated polyester composites: Effects on thermal-mechanical properties. J Dispers Sci Technol 39(8):1093–1101. https://doi.org/10.1080/01932691.2017.1382375
20. Alif Abdul Halim Z, Awang N, Azizi Mat Yajid M, Ahmad N, Hamdan H (2021) A comparison between the effects of hydrophobic and hydrophilic silica aerogel fillers on tensile and thermal properties of unsaturated polyester composites. Polym Bull. https://doi.org/10.1007/s00289-021-03798-4
21. Septevani AA, Evans DAC, Annamalai PK, Martin DJ (2017) The use of cellulose nanocrystals to enhance the thermal insulation properties and sustainability of rigid polyurethane foam. Ind Crops Prod 107:114–121. https://doi.org/10.1016/j.indcrop.2017.05.039
22. Chang KJ et al (2014) Preparation of silica aerogel/polyurethane composites for the application of thermal insulation. J Polym Res 21(1). https://doi.org/10.1007/s10965-013-0338-7
23. Wagh P et al (2015) Hydrophobicity measurement studies of silica aerogels using FTIR spectroscopy, weight difference method, contact angle method and K-F titration method. J Chem Biol Phys Sci 5(May):2350–2359
24. Merillas B, Villafañe F, Rodríguez-Pérez MÁ (2021) Nanoparticles addition in pu foams: The dramatic effect of trapped-air on nucleation. Polymers (Basel) 13(17):1–11. https://doi.org/10.3390/polym13172952
25. Nazeran N, Moghaddas J (2017) Synthesis and characterization of silica aerogel reinforced rigid polyurethane foam for thermal insulation application. J Non Cryst Solids 461:1–11. https://doi.org/10.1016/J.JNONCRYSOL.2017.01.037
26 Kausar A (2018) Polyurethane composite foams in high-performance applications: a review. Polym Plast Technol Eng 57(4):346–369. https://doi.org/10.1080/03602559.2017.1329433
27. Duarte I, Ferreira JMF (2016) Composite and nanocomposite metal foams. Materials 9:79. https://doi.org/10.3390/ma9020079
28. Yu YH, Choi I, Nam S, Lee DG (2014) Cryogenic characteristics of chopped glass fiber reinforced polyurethane foam. Compos Struct 107:476–481. https://doi.org/10.1016/J.COMPSTRUCT.2013.08.017
29. Kim JH, Ahn JH, Kim JD, Lee DH, Kim SK, Lee JM (2021) Influence of silica-aerogel on mechanical characteristics of polyurethane-based composites: Thermal conductivity and strength. Materials (Basel) 14(7). https://doi.org/10.3390/ma14071790
30. Son YM, Kim JD, Choi SW, Kim JH, Her NY, Lee JM (2019) Synthesis of polyurethane foam considering mixture blowing agents for application to cryogenic environments. Macromol Mater Eng 304(11). https://doi.org/10.1002/mame.201900294
31. Barikani M, Askari F, Barmar M (2010) A comparison of the effect of different flame retardants on the compressive strength and fire behaviour of rigid polyurethane foams. Cell Polym 29(6):343–358. https://doi.org/10.1177/026248931002900602
32. Konsago SW, Žiberna K, Kmet B, Benčan A, Uršič H, Malič B (2022) Chemical solution deposition of barium titanate thin films with ethylene glycol as solvent for barium acetate. Molecules 27(12). https://doi.org/10.3390/molecules27123753
33. Chirea M, Freitas A, Vasile BS, Ghitulica C, Pereira CM, Silva F (2011) Gold nanowire networks: Synthesis, characterization, and catalytic activity. Langmuir 27(7):3906–3913. https://doi.org/10.1021/la104092b
34. Cho J, Jang HG, Kim SY, Yang B (2019) Flexible and coatable insulating silica aerogel/polyurethane composites via soft segment control. Compos Sci Technol 171:244–251. https://doi.org/10.1016/J.COMPSCITECH.2018.12.027
35. Ahn JH et al (2019) Enhancement of mechanical and thermal characteristics of polyurethane-based composite with silica aerogel. Mater Sci Forum 951 MSF:63–67. https://doi.org/10.4028/www.scientific.net/MSF.951.63
36. Lee DI, Ha YH, Jeon H (2022) Preparation and Properties of Polyurethane Composite Foams with Silica-Based Fillers. Appl Sci 12(15):7418. https://doi.org/10.3390/app12157418
37. Kim JM et al (2018) Synthesis of nanoparticle-enhanced polyurethane foams and evaluation of mechanical characteristics. Compos Part B Eng 136:28–38. https://doi.org/10.1016/J.COMPOSITESB.2017.10.025